SAND2020-13732C

Computation and comparison of the stable northeastern United States marine boundary layer

Lawrence C. Cheung*
Sandia National Laboratories, Livermore, CA 94550

Shreyas Ananthan†, Michael J. Brazell‡, Ganesh Vijayakumar§, and
National Renewable Energy Laboratory, Golden CO 80401

Nathaniel B. deVelder¶ and Alan S. Hsieh.‖
Sandia National Laboratories, Albuquerque, NM 87185

In this work we investigate the behavior of stable marine boundary layers located near the coast of the Northeastern United States. Using the ExaWind large eddy simulation (LES) codes, three stable atmospheric conditions were chosen to match the Cape Wind measurements of Archer *et al.* with wind speeds of 5 m/s, 10 m/s, and 15 m/s at the 20 m measurement height. The behavior of the stable boundary layers, including mean flow quantities and turbulent statistics, are examined and compared to previous computations of the neutral and unstable offshore boundary layer at the same location. This study also examines the domain and mesh requirements necessary to capture the turbulent scales for the stable offshore boundary layers. Finally, we compare solutions computed using both Nalu-Wind and AMR-Wind solvers, and compare their predicted solutions and performance in this study.

I. Nomenclature

ABL	=	Atmospheric Boundary Layer
α	=	Wind shear exponent
β	=	Thermal expansion coefficient
c_p	=	Specific heat capacity
C_ϵ	=	Turbulence model constant
$\Delta, \Delta_{x,y,z}$	=	Grid spacing, grid spacing in x, y, z directions
ϵ_{ijk}	=	Levi-Civita symbol
f	=	Frequency
f_{max}	=	Maximum resolvable frequency due to mesh limits
f_{Ny}	=	Nyquist frequency
g, g_i	=	Gravitational acceleration
h	=	Enthalpy
k, TKE	=	Turbulent kinetic energy
L	=	Turbulent integral length scale
L_{Ob}	=	Obukhov length scale
ν_t	=	Turbulent viscosity
LES	=	Large Eddy Simulation
n_{dofs}	=	Number of degrees of freedom
n_r	=	Number MPI ranks
ϕ_h	=	Potential temperature gradient

*Principal member of technical staff, Thermal/Fluid Science & Engineering, AIAA member
†Researcher V, High-Performance Algorithms and Complex Fluids, AIAA Member
‡Researcher III, High-Performance Algorithms and Complex Fluids, AIAA Member
§Researcher III, Mechanical Engineering, AIAA Member
¶Postdoctoral appointee, Wind Energy Technologies Department, AIAA member
‖Senior member of technical staff, Wind Energy Technologies Department, AIAA member

q_j	=	Energy flux vector
ρ	=	Density
$\rho_\circ$	=	Reference density
Pr_t	=	Turbulent Prandtl number
R	=	Universal gas constant
R_{ij}	=	Two point correlation tensor
SBL	=	Stable Boundary Layer
S_i^u	=	ABL forcing source term
S_i	=	Wind spectra
σ_i	=	Wind speed variance
τ_{ij}	=	Stress tensor
θ	=	Potential temperature
T	=	Absolute temperature
TI	=	Turbulence intensity
t_{ts}	=	Time per time-step
$\overline{U}_{horiz}$	=	Time averaged horizontal velocity
u_i	=	Wind velocity in the i direction
u_τ	=	Friction velocity
V_1	=	Resolved wind speed at first grid level
Ω_i	=	Earth angular velocity vector

II. Introduction

The planned installation of several offshore wind energy plants in the United States has highlighted the need to properly understand the wind resource and atmospheric characteristics of the U.S. Atlantic Coast. Several atmospheric phenomena particular to this region, such as coastal low-level jets or seasonal Nor'easters, have the potential to substantially impact the operation and power production of offshore wind plants. Of particular interest to the current study is the atmospheric stability of the marine boundary layer in the Northeastern United States.

Atmospheric stability plays a large role in determining the power production of wind plants because it directly affects the vertical distribution of momentum and turbulent energy in the atmospheric boundary layer (ABL). The differences between the stable, neutral, or unstable stratified ABL can lead to large changes in wind speed or turbulence profiles, and ultimately change the operation of wind turbines. Atmospheric stability may also play a role in the formation of low-level jets [1] and cause increased fatigue loads on offshore wind turbines.

Several recent measurement campaigns have provided data to understand the ABL and wind characteristics for potential offshore wind farms in the Northeastern United States. Pichugina et al. [2] measured the wind profiles and vertical shear profiles in the Gulf of Maine using a ship-borne LIDAR approach. Analysis of measured data sets from Nantucket Sound by Archer et al. [3] showed a predominance of low-shear, unstable conditions at the site. However, strong seasonal variations and stratification changes due to diurnal variation were also observed.

A. Previous Simulation Work

In addition to these measurement campaigns, large eddy simulations (LES) have also been used to study ABL stability characteristics. Recent work by Kaul et al. [4] has shown that LES computations using Nalu-Wind can capture the neutral and convectively unstable onshore ABL. Previous simulations by Cheung et al. [5] successfully replicated the unstable and neutral ABL corresponding to the Cape Wind meteorological tower measurements [3] and showed the effects of surface heating on atmospheric stratification. LES of the stable ABL (SBL) presents certain challenges compared to neutral and convective stability states, stemming primarily from small dominant eddy length scales and low turbulence intensity. These challenges require higher resolution grids and/or advanced subgrid scale (SGS) models. As such, LES research of the SBL has been slower to evolve than the other stability states.

The first successful LES of the SBL was published by Mason and Derbyshire in 1990 [6]. They used a strategy of simulating a near steady-state neutral stability turbulent simulation, then added a cooling-surface boundary to develop the stable ABL. They recorded a need for implausibly strong initial perturbations to sustain turbulence using the Smagorinsky SGS model. Brown et al. [7] worked with Mason and Derbyshire to add stochastic backscatter to the SGS model, resulting in better agreement with surface layer observations. Andren [8] simulated two SBL types, one with a

neutral layer aloft, and one capped by an inversion, comparing two SGS models. He found significant improvements with the Sullivan SGS model, on par with the earlier backscatter model. Kemp and Thompson [9] used the same model as [7] to study particle dispersion, but the LES code did not replicate an expected plume growth. Derbyshire wrote a review of SBL modeling along with future projections in 1999 [10], noting the importance of local Richardson number and identifying a need to go to higher resolutions in SBL research.

In 2000, Kosovic and Curry [11] used an LES simulation with a nonlinear SGS model containing backscatter to favorably compare to the Beaufort Sea Arctic Stratus Experiment (BASE) measurements, showing that the SBL could reach a quasi steady-state. They also showed good agreement with the Nieuwstadt analytical model. In the same year, Saiki et al. [12] simulated an SBL with a strong capping inversion at z=500 m, producing reasonable surface layer profiles and identifying a need for SBL specific SGS models. Beare and MacVean [13] presented the first grid-focused work on LES of the SBL, using grids with deltas between 2 m and 12.5 m, finding significant variation between grid sizes. The inclusion of a backscatter model resulted in significant variation at a 6.25 m resolution, but very little at a 2 m resolution. Basu et al. [14] published a set of turbulence statistics, measurements, and LES simulations in support of the viability of Nieuwstadt's local scaling hypothesis under very stable conditions. Jimenez and Cuxart [15] set out to quantify the range for which standard SGS models, using the Kolmogorov theory for dissipation, were valid for increasingly stable flows. They found the model to perform adequately for weakly stable, and some moderately stable flow regimes.

An inter-comparison of LES simulations of the SBL was organized in 2006, the results of which are published in Beare et al. [16]. Collectively, this is known as the GABLS initiative, and involved simulating a moderately stable flow taken from Kosovic and Curry [11]. Eleven codes were compared in all, wherein grid deltas of less than 12.5 m were found to successfully maintain resolved turbulence, grid deltas less than 3.125 m showed little statistical change, and results became independent of SGS modeling at 1 m resolution. In the same year, Kumar et al. [17] successfully simulated an entire diurnal cycle with LES using a Lagrangian dynamic scale dependent SGS model. This model has been used by several researchers since 2011, including Lu and Porte-Agel [18], Huang and Bou-Zeid [19], Park et al. [20], and Abkar and Porte-Agel [21]. Stoll and Porte-Agel [22] compared three grid refinements and three scale dependent dynamic SGS models, showing that the Lagrangian and locally averaged models reproduced important flow features. The work of van Dop and Axelsen [23] provided even more evidence in support Nieuwstadt's local scaling hypothesis for SBLs. Chow and Zhou [24] showed evidence that the Smagorinsky model is simply too dissipative for use in strongly stable flows.

More recent work in LES of the SBL includes Matheou [25] who explored a large parameter space using the Smagorinsky-Lilly SGS closure, as well as Sullivan et al. [26]. Several researchers have applied SBL simulation in the wind energy space [21, 27, 28]. In 2020, Wurps et al. [29] provided a rigorous grid resolution study for the SBL, looking at mean flow, turbulence variables, and two-point correlations, using a dynamic SGS model that allows backscatter. They found grid requirements to be 2.5 m, 10 m, and 20 m for stable, neutral, and convective boundary layers respectively. They advocate looking at two point correlations in order to quantify flow structure size, which in turn provides a basis for evaluating grid resolution. In all of the reviewed literature, SBL LES has been run in the onshore context only; a complete comparison including offshore stable ABL conditions has yet to be completed.

B. Objectives

In the current study on stable marine boundary layers, we aim to build on the previous work in the literature and complete several objectives. First, we examine the domain and mesh requirements necessary to capture the turbulent scales for the stable offshore boundary layers. Secondly, two incompressible-flow LES solvers within the ExaWind simulation suite will be compared in this study: The unstructured-grid solver Nalu-Wind and the structured, adaptive mesh refinement (AMR) solver AMR-Wind. Both codes are used to calculate the same SBL, and the relative differences between the codes are reported. Finally, a series of stable boundary layer conditions will be computed using AMR-Wind that match the measurements of Archer et al. [3]. The behavior of the stable boundary layers, including mean flow quantities and turbulent statistics, are examined and compared to the neutral and unstable cases computed in [5].

Table 1 Measured conditions at Cape Wind. The stable atmospheric conditions used in this study are highlighted in bold below, while the neutral and unstable conditions from [5] are included for comparison.

Stability	Wind speed [m/s]	Wind dir [deg]	Turbulence intensity
Neutral	5	225	0.055
Neutral	10	225	0.055
Neutral	15	225	0.065
Unstable	5	315	0.080
Unstable	10	315	0.075
Unstable	15	315	0.090
Stable	**5**	**225**	**0.045**
Stable	**10**	**225**	**0.050**
Stable	**15**	**225**	**0.060**

III. Methodology

A. Measured offshore conditions

Following the work of Cheung et al. [5], we use measurements of the offshore coastal marine boundary layer, collected by the Cape Wind meteorological tower in Nantucket Sound, as the basis for this computational study. The Cape Wind platform collected wind measurements at 20 m, 41 m, and 60 m above the mean water level, along with temperature and barometric measurements from the years 2003-2011. From the observations, Archer et al. [3] found that the marine boundary layer is predominantly unstable, with 61% of conditions were classified as unstable, versus 21% neutral and 18% stable. The stratification of the marine boundary layer, as determined by the Obukhov length, also had a large impact on the wind speed profile, with flatter, non-logarithmic profiles seen during unstable conditions.

From the measured distribution of atmospheric stabilities, turbulent kinetic energies (TKE), and wind speeds from the Cape Wind platform at z=20 m, a stable set of conditions were chosen as targets for this computational study. A summary of the conditions for all stability classes is given in Table 1. In this work we focus on the three stable atmospheric conditions at wind speeds of 5 m/s, 10 m/s, and 15 m/s, while the neutral and unstable conditions where studied in previous work [5].

To maintain consistency with the measured data, the turbulence intensity (TI) is calculated using the TKE as

$$\mathrm{TI} = \frac{\sqrt{\frac{2}{3} \times \mathrm{TKE}}}{\overline{U}_{horiz}} = \frac{\sqrt{\frac{1}{3}\left(\overline{u_1' u_1'} + \overline{u_2' u_2'} + \overline{u_3' u_3'}\right)}}{\overline{U}_{horiz}}, \tag{1}$$

where u_i' is the fluctuating wind velocity in the i direction. The averaged wind speeds were enforced at the measurement height of 20 m, and the applied wind directions were consistent with the predominant stable direction of 225 degrees southwest.

B. Computational methodology and LES formulation

Large Eddy Simulations of the stable atmopsheric conditions described in Table 1 are performed using the open-source, ExaWind simulation environment*. ExaWind is a suite of high-fidelity modeling tools for analyzing complex microscale atmospheric boundary layer flows and wind farm flows. The present study uses two different incompressible computational fluid dynamic solvers available within the ExaWind suite, Nalu-Wind † and AMR-Wind ‡. This section briefly describes the incompressible Navier-Stokes equations solved, the specifics of the turbulence model and the wall shear stress formulation used to model the terrain, and the details of the numerical discretization in the two codes.

*https://github.com/exawind
†https://github.com/exawind/nalu-wind
‡https://github.com/exawind/amr-wind

1. Governing equations

Both computational fluid dynamics (CFD) codes solve the incompressible form of the Navier-Stokes equations with appropriate models for turbulence closure. Equation 2 shows the continuity and momentum equations with all the terms necessary to model the atmospheric boundary layer problem. LES filtered variables are denoted using the operation $(\bullet)$. Term **I** represents the pressure gradient forces as a deviation from hydrostatic and horizontal mean gradients, term **II** represents the contribution from viscous and sub-filter scale stresses, term **III** represents the contribution from Coriolis forces due to earth's rotation, term **IV** represents the effects of buoyancy, and term **V** represents source terms necessary to drive the flow to a desired horizontal mean velocity at prescribed heights.

$$\begin{aligned} \frac{\partial u_j}{\partial x_j} &= 0 \\ \frac{\partial}{\partial t}\left(\rho\, u_i\right) + \frac{\partial}{\partial x_j}\left(\rho\, u_i u_j\right) &= \underbrace{-\frac{\partial p'}{\partial x_j}\delta_{ij}}_{\mathbf{I}} \underbrace{-\frac{\partial \tau_{ij}}{\partial x_j}}_{\mathbf{II}} \underbrace{-2\rho\,\epsilon_{ijk}\,\Omega_j u_k}_{\mathbf{III}} + \underbrace{\left(\rho-\rho_\circ\right) g_i}_{\mathbf{IV}} + \underbrace{S_i^u}_{\mathbf{V}} \end{aligned} \tag{2}$$

For the simulations presented in this paper, the buoyancy term (**IV**) is approximated using the Bousinessq model. The Bousinessq model ignores the effect of density gradients on inertia while retaining its effects on buoyancy. The density fluctuations governing the buoyancy effects are approximated as

$$\frac{\rho}{\rho_\circ} \approx 1 - \beta\left(\theta - \theta_\circ\right) \tag{3}$$

This leads to a forcing term that depends on potential temperature (θ), the reference density $\rho_\circ = \rho$, and thermal expansion coefficient $\beta \approx 1/\theta_\circ$ as

$$\left(\rho - \rho_\circ\right) g_i = -\rho_\circ\, \beta\, g_i \left(\theta - \theta_\circ\right) \tag{4}$$

For ABL problems, the conservation of energy equation is usually written in terms of potential temperature as shown in Eq. 5.

$$\frac{\partial}{\partial t}\left(\rho\,\theta\right) + \frac{\partial}{\partial x_j}\left(\rho\, u_j \theta\right) = -\frac{\partial}{\partial x_j}\hat{q}_j \tag{5}$$

Under the assumption of ideal gas conditions and constant specific heat capacity c_p, the gradients in potential temperature are proportional to the gradients in absolute temperature, i.e.,

$$\left[\frac{\partial T}{\partial t}, \frac{\partial T}{\partial x}, \frac{\partial T}{\partial y}\right] = \left(\frac{\bar{p}}{p_\circ}\right)^{\left(\frac{R}{c_p}\right)} \left[\frac{\partial \theta}{\partial t}, \frac{\partial \theta}{\partial x}, \frac{\partial \theta}{\partial y}\right] \tag{6}$$

Furthermore, ignoring the pressure and viscous work terms, for incompressible flows, it can be shown that solving the enthalpy equation is equivalent to solving the potential temperature equation. The enthalpy equation solved in Nalu-Wind for wind energy problems is shown below

$$\frac{\partial}{\partial t}\left(\rho\, h\right) + \frac{\partial}{\partial x_j}\left(\rho\, u_j h\right) = -\frac{\partial}{\partial x_j} q_j. \tag{7}$$

It is noted here that the terms $\hat{q}_j$ (Eq. 5) and q_j (Eq. 7) are not equivalent and must be scaled appropriately. Users can still provide the appropriate initial and boundary conditions in terms of potential temperature field. Under these assumptions and conditions, the resulting solution can then be interpreted as the variation of potential temperature field in the computational domain.

The subgrid-scale kinetic energy (k) one-equation turbulence model (Eq. 8), based on Moeng [30], is used for LES turbulence closure,

$$\frac{\partial}{\partial t}\left(\rho k\right) + \frac{\partial}{\partial x_j}\rho k u_j = \frac{\partial}{\partial x_j}\left(2\nu_t \frac{\partial k}{\partial x_j}\right) - 2\nu_t S_{ij} S_{ij} + \frac{g}{\theta_\circ}\tau_{\theta_i} - C_\epsilon \frac{k^{3/2}}{l} \tag{8}$$

where

$$C_\epsilon = 0.93 \qquad \nu_t = C_\epsilon l\sqrt{k}$$

$$\tau_{\theta i} = -2\,\frac{\nu_t}{\mathrm{Pr}_t}\,\frac{\partial\theta}{\partial x_i} \qquad \mathrm{Pr}_t = \left(1 + \frac{2l}{\Delta}\right)^{-1}$$

The choice of the length scale (l) depends on whether the stratification is positive or negative, based on the recommendation by Moeng [30], and is given by

$$l = \begin{cases} \Delta = \sqrt[3]{\Delta_x\Delta_y\Delta_z}, & \frac{\partial\theta}{\partial z} < 0, \\ 0.76\,\sqrt{k}\,\frac{g}{\theta_\circ}\left(\frac{\partial\theta}{\partial z}\right)^{-1/2}, & \frac{\partial\theta}{\partial z} > 0. \end{cases} \tag{9}$$

2. Lower wall model BC

The sub-filter scale stresses are specified at the terrain boundary following Moeng [30] as

$$(\tau_{xz})_0 = \langle\tau_{xz}\rangle_0 \frac{V_1\langle u_1\rangle + \langle V_1\rangle(u_1 - \langle u_1\rangle)}{\langle V_1\rangle\sqrt{\langle u_1\rangle^2 + \langle v_1\rangle^2}}, \tag{10}$$

$$(\tau_{yz})_0 = \langle\tau_{yz}\rangle_0 \frac{V_1\langle v_1\rangle + \langle V_1\rangle(v_1 - \langle v_1\rangle)}{\langle V_1\rangle\sqrt{\langle u_1\rangle^2 + \langle v_1\rangle^2}}, \tag{11}$$

$$(\tau_{\theta z})_0 = \langle\tau_{\theta z}\rangle_0 \frac{V_1(\langle\theta_1\rangle - \theta_\circ) + \langle V_1\rangle(\theta_1 - \langle\theta_1\rangle)}{\langle V_1\rangle(\langle\theta_1\rangle - \theta_\circ)}, \tag{12}$$

where all quantities with the subscript 1 are values at the first vertical grid level, V_1 is the resolved wind speed at the first grid level and $\langle\bullet\rangle$ represents the horizontal plane average at that height. The mean sub-filter stresses are computed using the Monin-Obukhov similarity law [31]. The formulation for the potential temperature flux could potentially experience a singularity when the mean resolved potential temperature at the first grid level $\langle\theta_1\rangle$ crosses the reference temperature $\theta_\circ$. Hence the model for the sub-filter potential temperature flux is reformulated using the Monin-Obukhov similarity law as

$$(\tau_{\theta z})_0 = \left(\frac{u_\tau\kappa}{\phi_h}\right)\frac{V_1(\langle\theta_1\rangle - \theta_\circ) + \langle V_1\rangle(\theta_1 - \langle\theta_1\rangle)}{\langle V_1\rangle}, \tag{13}$$

where ϕ_h is the non-dimensional potential temperature gradient from Monin-Obukhov similarity law [31].

3. Nalu-Wind

Nalu-Wind [32] is an open-source, wind-focused fork of the Nalu CFD code [33]. The codebase heavily leverages the open-source Trilinos suite of numerical libraries [34]. Nalu-Wind uses an unstructured-grid, node-centered, finite-volume formulation for solving the incompressible Navier-Stokes equations. Two spatial discretization approaches are supported within the codebase: the edge-based scheme and control-volume finite-element scheme. The edge-based scheme, used in the present study, is similar to the classical cell-centered finite volume formulation formulated on a dual volume surrounding the nodes of the mesh. The governing equations are discretized in time using a split-operator approach. An implicit backward difference formula (BDF2) time-stepping algorithm with an approximate pressure projection scheme [35] is used to advance the equations in time. Multiple Picard-style outer-loop iterations are employed within each time step to minimize the errors introduced from split-operator approximations. Nalu-Wind comes equipped with a suite of Reynolds-Averaged Navier-Stokes (RANS), LES, and Detached Eddy Simulation (DES) turbulence models to resolve the disparate spatial and temporal scales encountered when modeling wind plant flows.

Nalu-Wind heavily utilizes the Sierra Toolkit (STK) library [36] for managing the unstructured mesh data structures. The linear systems resulting from the discretized equations are solved using solvers available within the Belos and MueLu libraries within Trilinos. The momentum and scalar transport equations are solved using GMRES iterative solvers with symmetric Gauss-Seidel (SGS) preconditioners. The elliptic pressure Poisson equation is solved using GMRES solvers with a smoothed-aggregated algebraic multigrid preconditioner. The reader is referred to Sprague et al. [32] and Domino [33] for more details.

While the primary objective of Nalu-Wind within the ExaWind simulation suite is to support blade-resolved simulations of wind turbines, it comes equipped with all the physics models necessary for modeling atmospheric

Table 2 LES parameters for stable ABL conditions

Stability	Wind speed	Surface roughness z_0	Surface temperature change	Time step
Stable	5 m/s	0.0005 m	-0.32 K/hr	0.25 sec
Stable	10 m/s	0.0005 m	-1.40 K/hr	0.125 sec
Stable	15 m/s	0.0005 m	-1.50 K/hr	0.0625 sec

boundary flows. In the present work, the prognostic equation for temperature is solved using the enthalpy equation (Eq. 7). The prognostic one-equation, subgrid-scale kinetic energy equation (Eq. 8) is used for LES turbulence closure. Two Picard iterations were employed within each time step to reduce splitting errors and improving time accuracy.

4. AMR-Wind

As part of a suite of physics codes within the open-source ExaWind simulation environment, AMR-Wind enables more efficient and scalable simulations of wind power plants. This is because it is built on top of the AMReX software framework, which contains all of the functionality needed to develop massively parallel, block-structured adaptive mesh refinement (AMR) applications [37]. Because AMR-Wind is limited to Cartesian block-structured grids, it is specialized to handle ABL physics and wind turbine wakes. The block-structured grids enable more efficient algorithms such as Multi-Level Multi-Grid (MLMG) [37] and are well suited for next generation supercomputers that use graphical processing units (GPUs). In the current work, we focus on applying AMR-Wind to ABL computations using statically refined, uniform meshes, and will examine adaptive mesh capabilities in future studies.

AMR-Wind solves the incompressible Navier-Stokes equations and is generalized to handle variable density and viscosity. Additionally, scalar transport equations can be solved, such as potential temperature or turbulence models. The discretization in AMR-Wind is based on the approximate projection method used in IAMR [38] and incflo [39]. It is a semi-staggered scheme where the velocity and scalar variables are located at cell centers and pressure is located at nodes. Pressure is also staggered in time so that pressure and the pressure gradient (located at cell centers) are at time $n + 1/2$. The time discretization is handled with a Crank Nicolson approach where the right-hand side of the system of equations is evaluated at time $n + 1/2$. The advection term is handled explicitly using an upwind finite-volume method. There are multiple options within AMR-Wind, but in this paper only the high-order Godunov Piecewise Parabolic Method (PPM) is used [40]. The advection terms are projected to face centers at $n + 1/2$ and are corrected using an exact MAC projection [38], which guarantees a divergence-free flow. The diffusion terms can be handled explicitly, semi-implicitly, or implicitly and are spatially discretized using a second-order central difference formula. For the simulations in this paper, we use an implicit scheme for the viscous terms, as the variable viscosity from the eddy viscosity may cause time step restrictions. After the scalar equations and the momentum equations are advanced in time, a nodal projection is used to approximately correct the velocity field to make it divergence free. The nodal projection is based on a node centered finite element method [38].

C. Computational setup

The computational methodology for the AMR-Wind and Nalu-Wind LES codes follows practices similar to the previous offshore ABL study [5], with some modifications to handle the stable stratification. As in [5], the domain was a square prism geometry, with the x and y coordinates aligned in the East and North directions, respectively. The domain size and mesh requirements were determined through a numerical grid study. As discussed in section IV.A, the horizontal dimensions of 750 m $\times$ 750 m were found to be sufficient to capture any large scale structures in the boundary layer, and in all cases the vertical dimension of 1000 m was also used. The grid study in section IV.A also showed that the stable stratification required greater mesh refinement to capture the smaller turbulent scales, and a uniform cell size of 2.5 m was adopted for the offshore LES computations across both codes.

Momentum source terms were included in Nalu-Wind and AMR-Wind to ensure that the horizontally averaged velocity matched the targeted wind speed at the z=20 m height. These source terms are based on the difference between the desired wind velocity and the instantaneous horizontally averaged velocity, and are only a function of time and height z. Coriolis forcing matching the Cape Wind latitude was included to capture the effect of wind change with elevation.

Table 3 The setup for the grid resolution study

Case	Δ_x	Δ_y	Δ_z	Domain size
Nalu-Wind coarse	10.0 m	10.0 m	2.5 m	1.5 km × 1.5 km × 1.0 km
Nalu-Wind medium	5.0 m	5.0 m	2.5 m	1.5 km × 1.5 km × 1.0 km
Nalu-Wind fine	2.5 m	2.5 m	2.5 m	1.0 km × 1.0 km × 1.0 km

1. Boundary and initial conditions

In both horizontal directions of the computational domain, periodic boundary conditions were applied. At the lower boundary, we chose to represent the air/ocean interface using flat boundary with small amount of surface roughness. This allowed the wall model discussed in section III.B.2 to be applied. Monin-Obukhov similarity theory was used to determine the velocity and temperature profiles near the lower surface given a surface roughness height z_0 and the prescribed surface temperature as a function of time. At the upper surface of the domain, a potential flow based boundary condition is applied along with a normal temperature gradient of 0.003 K/m.

The initial temperature profile in all cases was a constant 300 K until the specified inversion height of 650 m. The inversion layer thickness was 100 m, and above this, the temperature linearly increased until it reached 308.75 K at the upper boundary. The initial mean velocity profile was uniform throughout the domain with superimposed sinusoidal velocity perturbations of magnitude 1 m/s to promote the development of turbulence.

2. Determination of surface roughness and prescribed temperature

To match the measured TI conditions given in Table 1, the surface roughness and prescribed surface temperature change were adjusted through an initial trial-and-error process. The final surface roughness of z_0=0.0005 m used for the stable offshore conditions (see Table 2) matched the roughness used in the neutral 15 m/s and unstable 5 m/s and 10 m/s cases from the previous study [5]. This value of surface roughness is consistent with the measurements from the North Sea [41], which found values of z_0 ranging from 5×10^{-5}m to 5×10^{-3} m.

The values of the prescribed temperature change at the ocean surface is also given in Table 2. As the wind speed increases, a larger temperature decrease was used to maintain similar levels of stable stratification, as expected from Monin-Obukhov similarity theory.

Once the appropriate surface roughness and prescribed temperature were determined, and the correct mesh requirements known from the study in section IV.A, the LES computations for the stable 5 m/s, 10 m/s, and 15 m/s ABL cases could be set up and run. Each of the cases was run for 15,000 seconds before collecting statistics for another 5,000 seconds. To maintain a CFL number less than unity during these runs, a smaller time step was used for the higher wind speeds (see Table 2).

IV. Results

A. Domain and mesh resolution study

In order to ensure that the large and small turbulence scales were properly resolved in the offshore LES simulations, the appropriate domain size and mesh resolution needed to be determined. Under-resolved meshes or domain sizes that are too small may miss the smaller turbulence scales or remove the larger structures required for proper ABL development. However, over-resolved meshes or unnecessarily large domains might lead to excessive computational requirements to complete the simulations.

To determine the appropriate mesh size and resolution, a grid study was conducted using the stable 5 m/s ABL case and the Nalu-Wind code. A number of cases were set up using the surface roughness and prescribed temperature decreases listed in Table 2, but with varying grid resolutions and conservative estimates for the domain size required. As shown in table 3, the horizontal resolutions varied from 10 m to 2.5 m cells for the coarse and fine cases, respectively. All simulations for the grid study also used a vertical resolution of Δ_z=2.5 m and the same vertical extent of 1 km.

Note that in this paper, we focus our attention on the horizontal resolution required to resolve key physical features in the SBL, and some additional impacts deserve additional study. For instance, the impact of non-isotropic meshes with the k-sgs turbulence model and wall function treatment is not addressed here and worthy of additional attention.

The suitability of these meshes and domain sizes were determined based on the resulting wind spectra and turbulent

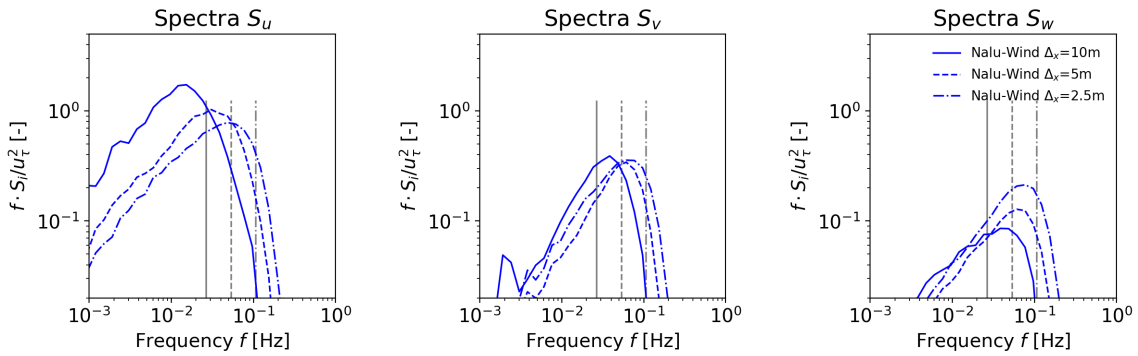

Fig. 1 Calculation of the wind spectra S_i for LES of stable 5 m/s case with different resolutions. The gray vertical lines correspond to the maximum resolvable frequency f_{max} according to equation (16).

correlation metrics from the simulated ABL. The wind spectra $S_i(f)$ is defined as a function of the frequency f

$$\int_0^\infty S_i(f)\mathrm{d}f = \sigma_i^2, \tag{14}$$

where σ_i is the wind speed variance and the index $i = u, v, w$ denotes the longitudinal, lateral, or vertical velocity, respectively. For the LES simulations in this study, we desire that the mesh resolution be sufficiently fine to capture the high frequency components of the spectra past the spectral peak. This helps ensure that the unsteady characteristics in the boundary layer are resolved.

Two numerical constraints limit the maximum resolvable frequency in the current ABL computations. First, the Nyquist frequency f_{Ny} limits the highest resolved frequency to half the sampling frequency, or

$$f_{Ny} = \frac{1}{2 \times \mathrm{dt}}. \tag{15}$$

Secondly, the maximum resolvable frequency of convecting fine scale eddies on a mesh with grid size Δ and average horizontal wind speed $\bar{U}_{horiz}$ can be estimated as

$$f_{max} = \frac{0.6\bar{U}_{horiz}}{N\Delta}. \tag{16}$$

Here, Eq. 16 assumes that the turbulent eddies convect with a velocity of $0.6\bar{U}_{horiz}$ and $N = 8$ is chosen for the purposes of this study. Due to the alignment of the flow with the mesh directions, the grid size is defined as $\Delta = \sqrt{2}\Delta_x$. In all cases considered here, $f_{max} < f_{Ny}$, so the limiting constraint for resolving the high frequency components was the mesh resolution.

The comparison of the wind spectra and maximum resolvable frequency f_{max} for the different mesh resolutions is shown in Figure 1. Here spectra is shown at the z=20 m height and averaged using 1/3 octave-bins to enhance clarity. For the S_u and S_w spectra, there are noticeable shifts in the peak amplitude, while the peak amplitudes for S_v remained fairly constant between cases. In all cases, the peak frequency of $S_i(f)$ also increased as the resolution increased. While the mesh resolution was sufficient to capture the peak frequency for S_u, the fine resolution with 2.5 m mesh cells was required to capture the spectral peaks for the lateral and vertical velocities.

However, the above analysis of spectra only provides information to determine if the turbulent fluctuations can be resolved temporally, and a separate analysis is needed to determine if the fluctuations can be resolved in different spatial directions. The second metric for examining the appropriate grid size and mesh resolution is through the correlation tensor and turbulence integral length scale. The two-point correlation tensor $R_{ij}(\mathbf{x}, \boldsymbol{\xi})$ at position $\mathbf{x}$ and separation vector $\boldsymbol{\xi}$ is defined as

$$R_{ij}(\mathbf{x}, \boldsymbol{\xi}) = \frac{\overline{u_i'(\mathbf{x}, t)u_j'(\mathbf{x} + \boldsymbol{\xi}, t)}}{\sqrt{\overline{u_i'^2}}\sqrt{\overline{u_j'^2}}}, \tag{17}$$

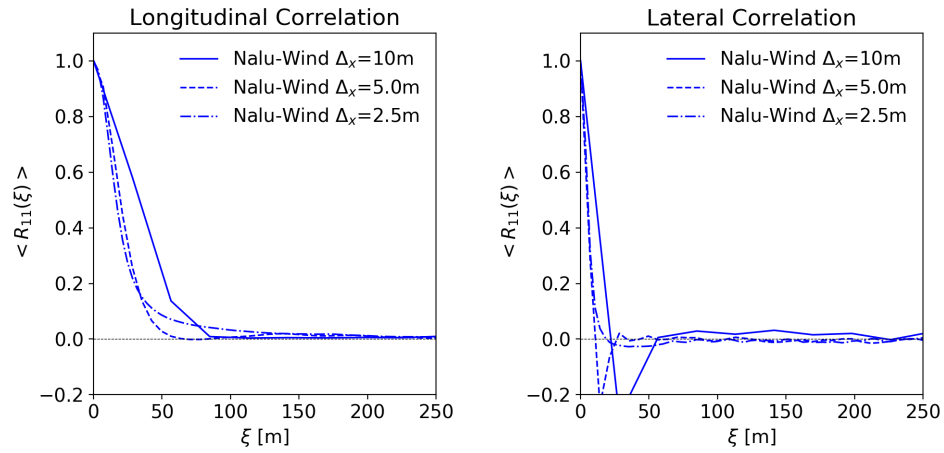

Fig. 2 Calculation of the averaged longitudinal and lateral $\langle R_{11}(\boldsymbol{\xi})\rangle$ coefficients at z=20 m for LES of stable 5 m/s case with different resolutions.

where the velocity fluctuations u_i' are defined as

$$u_i'(\mathbf{x}, t) = u_i(\mathbf{x}, t) - \overline{u_i(\mathbf{x}, t)}, \tag{18}$$

and the overbar operator $\overline{(\bullet)}$ denotes time averaging. In the current study, we compute the horizontally averaged correlation coefficient $\langle R_{11}(\boldsymbol{\xi})\rangle$ by sampling over multiple points at the z=20 m height, typically 100-150 points, and averaging the result. The longitudinal $\langle R_{11}(\boldsymbol{\xi})\rangle$ was calculated by looking at separation vectors $\boldsymbol{\xi}$ in the streamwise direction while the lateral $\langle R_{11}(\boldsymbol{\xi})\rangle$ used separation distances $\boldsymbol{\xi}$ which were orthogonal to the wind direction on the same horizontal plane.

The results shown in Figure 2 show that the finest resolution is required to resolve both the longitudinal and the lateral length scale. In contrast to the neutral and unstable ABL cases, the turbulent structures decorrelate rapidly and are noticeably finer in the lateral direction compared to the longitudinal direction. While 2.5 m resolution is adequate to resolve the longitudinal turbulent structures, the lateral direction may require even finer resolution to fully resolve. This may be an important consideration in situations where turbulence in a SBL interacts with turbine features, such as blade motions or downstream wakes. However, the additional refinement requires careful balancing against the additional computational expense in the simulation.

Additional information about the mesh and domain requirements can be drawn by examining the turbulent integral length scale L. This length scale can be calculated from $\langle R_{11}(\boldsymbol{\xi})\rangle$ via

$$L = \int_0^\infty \langle R_{11}(\xi)\rangle \, \mathrm{d}\xi, \tag{19}$$

and the results are shown in Table 4. With a resolution of 2.5 m, the ratio of the longitudinal length scale to the grid size $L/\mathrm{d}x \approx 10.1$, while in the lateral direction $L/\mathrm{d}x \approx 2.36$, suggesting even finer resolution is required to capture the lateral scales. This may be a critical consideration when resolving both the lateral and longitudinal turbulent scales are important, such as in SBL simulations with turbine interactions. However, in other situations, the additional computational cost incurred may be prohibitive and only the longitudinal component can be resolved.

Based on the longitudinal length scale, we also determined the overall domain size necessary for stable ABL calculations. To provide sufficient space to ensure development and decorrelation of turbulent structures, domain sizes of approximately 10 times the longitudinal length scale is recommended. However, the inclusion of sample probes with sufficient separation distance to accurately calculate $\langle R_{11}(\boldsymbol{\xi})\rangle$ roughly doubles the domain size requirements. Assuming longitudinal length scales on the order of 30 m, we estimated a minimum domain size of 750 m $\times$ 750 m in the horizontal directions for both the Nalu-Wind and AMR-Wind LES calculations.

Table 4 The calculated turbulent integral length scale for each of the grid resolutions

Case	Δ_x	Longitudinal L	Lateral L
Nalu-Wind coarse	10.0 m	36.4 m	0.0 m
Nalu-Wind medium	5.0 m	21.5 m	4.52 m
Nalu-Wind fine	2.5 m	25.3 m	5.92 m

Table 5 Comparison of AMR-Wind and Nalu-Wind ABL statistics

Code	Wind speed	TI	α	u_τ
Nalu-Wind	5 m/s	0.0481	0.165	0.163 m/s
AMR-Wind	5 m/s	0.0483	0.166	0.157 m/s

B. Comparison of AMR-Wind versus Nalu-Wind

Before examining the behavior of offshore ABL across all wind speeds, we first compare the results for a single case using both LES codes. In this section, we consider the stable 5 m/s case, calculated in the same manner using both AMR-Wind and Nalu-Wind. Both LES codes used a mesh resolution of 2.5 m based on the guidance from section IV.A and the computational resources available.

After running each case for 15,000 s, the boundary layer statistics and horizontally averaged profiles were averaged for another 5,000 s. In Table 5, some mean statistics are given for both cases, including the friction velocity u_τ, the turbulence intensity TI at z=20 m, and local shear exponent α at z=20 m, defined as

$$\alpha = \frac{z}{U_{horiz}} \frac{dU_{horiz}}{dz}.$$

AMR-Wind and Nalu-Wind produced nearly identical values for the TI=0.048, which is close to measured target of 4.5%, and similar agreement was found for the shear exponent α. A minor descrepancy was found in the friction velocity u_τ, with AMR-Wind resulting in a value slightly lower than Nalu-Wind.

The comparison of the horizontally averaged wind profiles is shown in Figure 3. At the forcing height z=20 m, the wind speed and wind shear are close to an exact match between the two LES codes. The horizontal wind speeds continue to agree well for $z < 100$ m, beyond which a relatively constant velocity difference is observed. For both AMR-Wind and Nalu-Wind, an approximately linear veer profile was observed until $z \approx 250$ m, at which point the wind direction remained constant until the inversion layer height. The level of agreement between AMR-Wind and Nalu-Wind at the higher elevations is comparable to the inter-comparison of LES simulations Beare et al. [16], and may be improved through finer scale simulations which fully resolve the lateral turbulent lengthscales.

The computed TI and temperature profiles were observed to agree remarkably well between the LES codes. As shown in Figure 4, the stable ABL computed using AMR-Wind and Nalu-Wind both show a similar decay of turbulent kinetic energy with altitude z, and there is also little difference between the two temperature profiles $T(z)$.

In addition to the mean profiles described above, we also examined the wind spectra and turbulent correlation statistics from both AMR-Wind and Nalu-Wind for the stable 5 m/s case. A comparison of the computed wind spectra $S_i(f)$ from both LES codes is shown in Figure 5. At low frequencies, both AMR-Wind and Nalu-Wind predict similar spectral behavior, and both codes predict relatively similar spectral peaks for the S_v and S_w spectra. For the longitudinal spectra S_u, however, AMR-Wind predicts a slightly lower the peak amplitude than Nalu-Wind.

1. Computational efficiency

For the 5 m/s SBL case AMR-Wind had a median time of 0.27 s per time step. This means the entire simulation took about 6 hours to simulate 20000 s of physical time. For this case a total of $288 \times 288 \times 384$ cells were used which were solved in parallel using 972 MPI ranks. Simulations were carried out using NREL's Eagle supercomputer and AMR-Wind was compiled using Intel 2018. Typically on CPU's we see a strong scaling limit at around 15k cells per MPI rank. But for this case we used 32,768 cells per MPI rank which is about half the strong scaling limit. The time per degree of freedom for AMR-Wind is

$$\frac{n_r t_{ts}}{n_{dofs}} = 8.2 \times 10^{-6}[s]$$

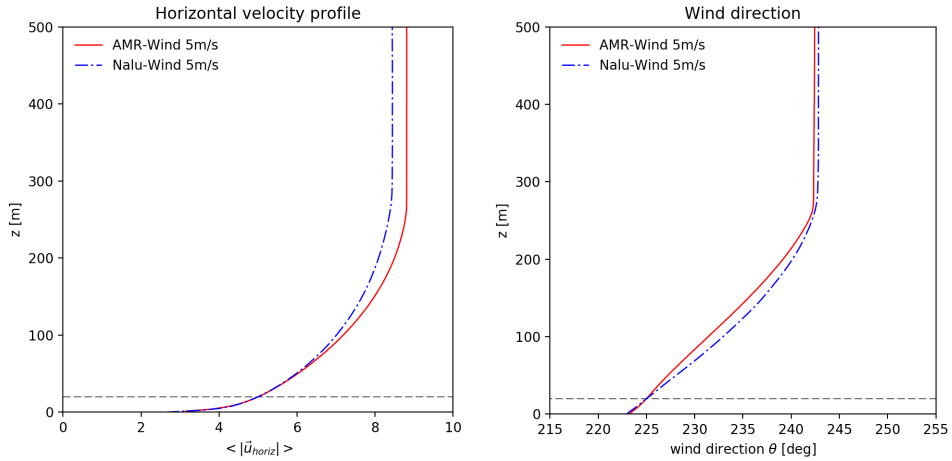

Fig. 3 Comparison of AMR-Wind and Nalu-Wind horizontal velocity and wind direction profiles for the stable 5 m/s boundary layer. The dashed horizontal line corresponds to the measurement height z=20 m.

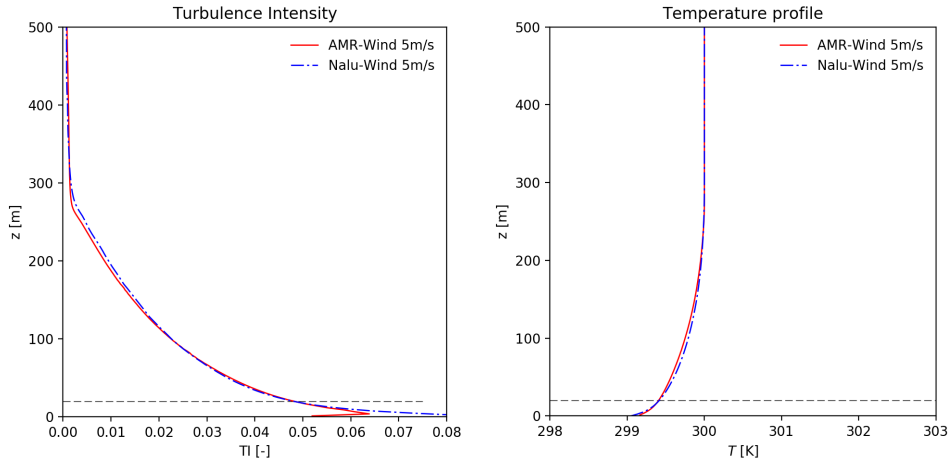

Fig. 4 Comparison of AMR-Wind and Nalu-Wind turbulence intensity and temperature profiles for the stable 5 m/s boundary layer. The dashed horizontal line corresponds to the measurement height z=20 m.

where n_r is the number of MPI ranks, t_{ts} is time per time step, and n_{dofs} is the total number of degrees of freedom (for AMR-Wind degrees of freedom are taken to be number of cells in the grid). This value allows us to compare speed relative to Nalu-Wind when using a different grid and number of MPI ranks, where a smaller value means a faster time to solution. It should be noted that the choice to use fewer elements for AMR-Wind was to ensure perfect load balancing across MPI ranks. This $288 \times 288 \times 384$ grid can be perfectly decomposed into smaller 32^3 blocks.

In comparison, the same case for Nalu-Wind takes 3.4 s per time step which takes about 75 hours to complete the simulation. This simulation was carried out on 1224 MPI ranks for a grid that contains $300 \times 300 \times 400$ cells. The equivalent time per degree of freedom for Nalu-Wind is 1.1×10^{-4} s, where degrees of freedom are the number of nodes in the mesh. For this case AMR-Wind is more than an order of magnitude faster per degree of freedom than Nalu-Wind. This significant speed difference is due to the use of structured grids in AMR-Wind compared with unstructured grids in Nalu-Wind. There are many benefits to using structured grids and for AMR-Wind this speed advantage is mostly attributed to the MLMG linear solver in the AMReX library [37]. This is because for each time step the computational work is dominated by solving two Poisson equations (MAC projection and nodal projection).

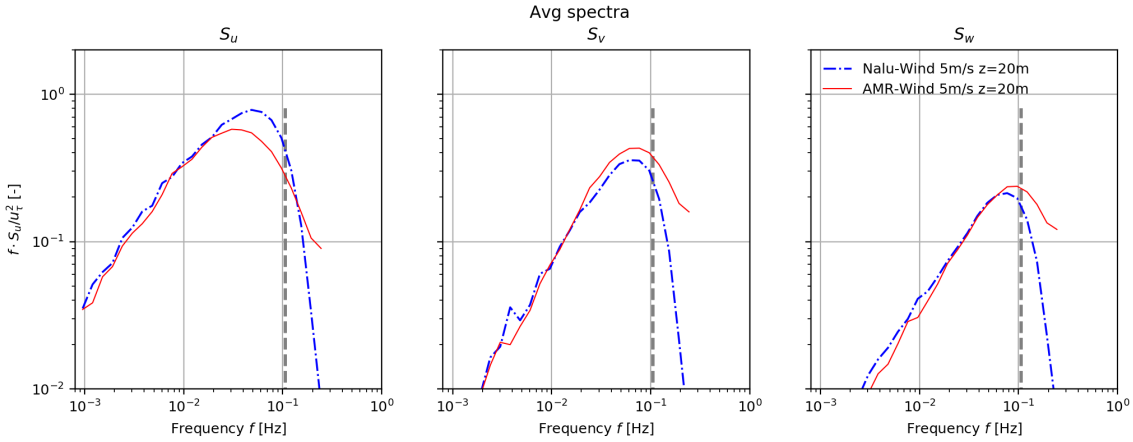

Fig. 5 Comparison of AMR-Wind and Nalu-Wind wind spectra at z=20 m for the stable 5 m/s boundary layer.

Table 6 Comparison of Stable ABL for all wind speeds

Code	Wind speed	TI	α	u_τ	Obukhov L_{Ob}	Longitudinal L	Stability
AMRWind	5 m/s	0.0483	0.166	0.157 m/s	52.5 m	27.7 m	Very stable
AMRWind	10 m/s	0.0506	0.160	0.319 m/s	57.2 m	29.6 m	Very stable
AMRWind	15 m/s	0.0550	0.118	0.511 m/s	131.3 m	43.8 m	Stable

C. Comparison of the stable offshore ABL for different wind speeds and stabilities

Using the results of the stable cases described in III.C, as well as the neutral and unstable ABL computations from the previous study in Cheung et al. [5], we can examine the influence of wind speed and stratification on offshore ABL behavior. In this section, we use the AMR-Wind code to calculate the stable ABL at 5 m/s, 10 m/s, and 15 m/s because of its computational efficiency and comparable accuracy to Nalu-Wind. From the results we first compare the differences between the three stable ABL cases, and then compare their behavior with the previously computed neutral and unstable counterparts.

1. ABL integrated quantities

From AMR-Wind LES calculations, a number of quantities can be computed to compare with the measured targets from Archer et al. [3]. In table 6, we list the TI, shear exponent α, friction velocity u_τ, Obukhov length L_{Ob}, longitudinal length scale L, and stability classification for each of these three cases. The TI values, calculated at the height z=20 m fall within the target range of 4.5% to 6.0% for stable conditions from the Cape Wind measurements. The calculated friction velocities are also similar to the values from the neutral offshore ABL calculations of [5], where u_τ varied from 0.15 m/s to 0.51 m/s for wind speeds of 5 m/s to 15 m/s.

The degree of stratification in each of the marine boundary layers can be quantified through the Obukhov length L_{Ob}, defined here as

$$L_{Ob} = -\frac{u_\tau^3 T_0}{\kappa g \langle \overline{w'T'} \rangle}, \tag{20}$$

where the κ=0.41 is the Kolmogorov constant, g is the gravitational acceleration, T_0 is the reference temperature, and $\langle \overline{w'T'} \rangle$ is the horizontally and time-averaged temperature flux. In this study we adopt the same classification guidelines as Archer et al [3], and identify boundary layer cases where $100 < L_{Ob} < 500$ as "stable," and cases where $5 < L_{Ob} < 100$ as "very stable." From the values listed in Table 6, we find that the lower wind speeds are "very stable," while the highest 15 m/s wind speed is classified as "stable." This is consistent with the measured Cape Wind distributions, where very stable conditions are more frequent than stable conditions at lower wind speeds, and gradually disappear beyond 13 m/s (c.f. Figure 5b in [3]).

2. Flow behavior and horizontally averaged profiles

The qualitative behavior of the stable boundary layers can be seen through snapshots of the flow taken from each of the simulations. In Figure 6, instantaneous snapshots of the horizontal and vertical velocities for each of the three cases at the z=20 m measurement height are shown. The largest difference can be seen in the size of the flow structures between the very unstable and stable cases. Longer streaks are evident in the 15 m/s case compared to the 5 m/s and 15 m/s cases, which is consistent with the nearly 50% larger integral length scale L given in Table 6. The differences in the vertical velocity are also evident in Figure 6. At higher wind speeds the magnitude of the vertical w' fluctuations increase, which plays a strong role in the growth of the boundary layer.

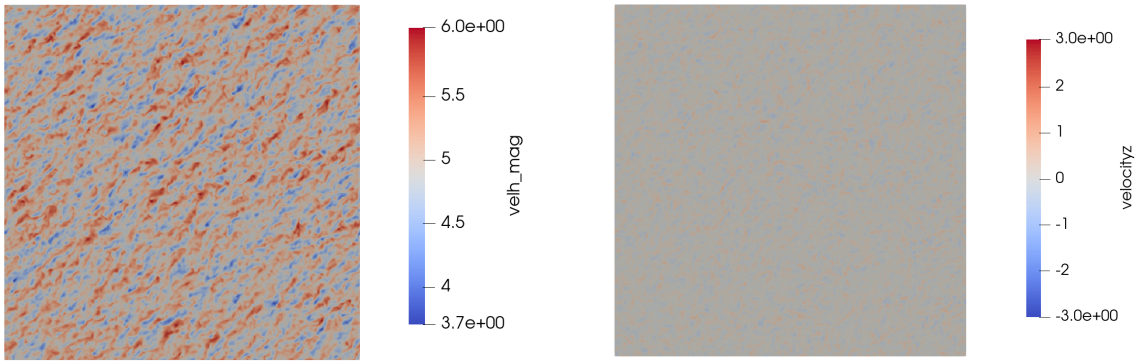

(a) horizontal vel., stable 5 m/s (b) vertical vel., stable 5 m/s

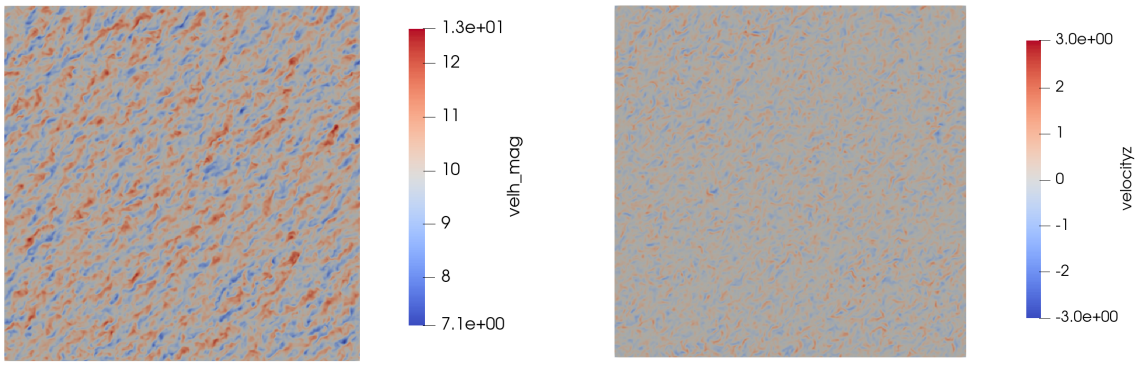

(c) horizontal vel., stable 10 m/s (d) vertical vel., stable 10 m/s

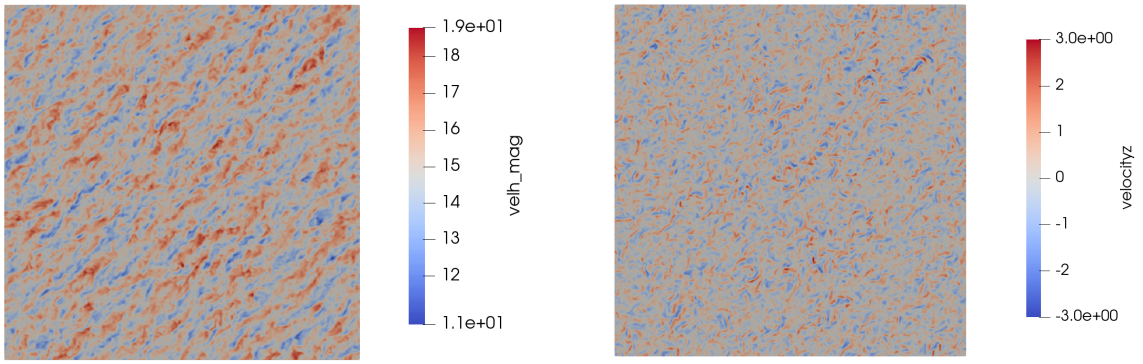

(e) horizontal vel., stable 15 m/s (f) vertical vel., stable 15 m/s

Fig. 6 Snapshots of the horizontal velocity and vertical velocity, taken at t=20,000 s of the simulations at height z=20 m, for the AMR-Wind calculation of the stable 5 m/s, 10 m/s, and 15 m/s ABL.

This observation can also be seen in images taken along the flow direction 225°, as shown in Figure 7. At the time

t=20,000 s, the growth of the of 15 m/s stable boundary layer is considerably larger than the very stable 5 m/s and 10 m/s cases, and has nearly reached the inversion layer height. To reach the same level of boundary layer growth, the very stable ABL cases would require longer simulation times, possibly longer than the nighttime conditions measured experimentally.

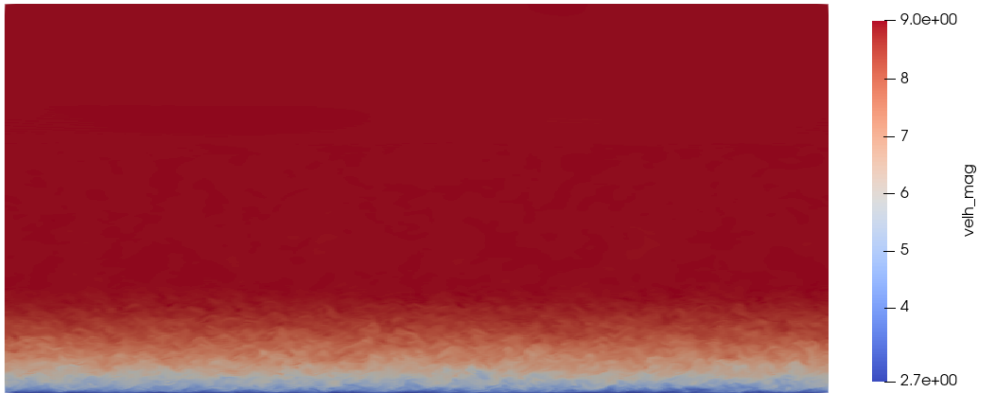

(a) AMR-Wind stable, 5 m/s

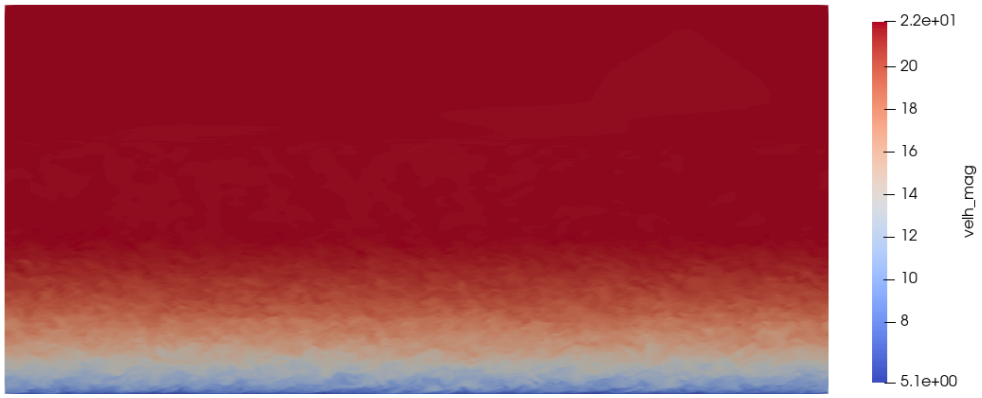

(b) AMR-Wind stable, 10 m/s

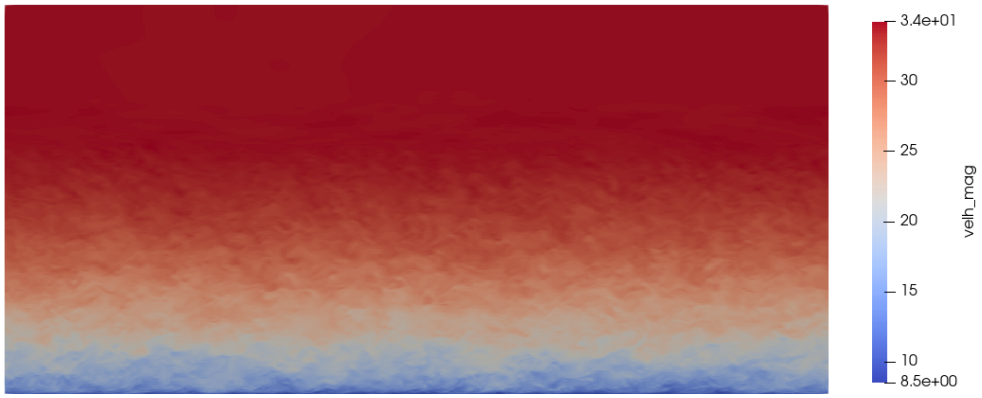

(c) AMR-Wind stable, 15 m/s

Fig. 7 Snapshots of the horizontal velocity, taken at t=20,000 s along the wind direction, for the (a) 5 m/s, (b) 10 m/s, and (c) 15 m/s AMR-Wind stable calculations

Horizontally averaged flow profiles shown in Figures 8 and 9 provide a more quantitative assessment of the ABL evolution. The rapid growth of the 15 m/s stable case leads to strong shear throughout the boundary layer up to the inversion height, while the very stable 5 m/s and 10 m/s cases showed minimal shear at higher elevations (Figure 8). The change in wind direction is also indicative of the boundary layer penetration. Approximately linear veer profiles are visible up to heights of z ≈250 m and z ≈350 m for the 5 m/s and 10 m/s cases, respectively, while the linear veer is present in the 15 m/s stable case up to z=650 m.

The behavior of the TI and temperature profiles in Figure 9 closely follows the shear and veer profiles discussed above. Despite all cases reaching similar TI levels at z=20 m, the turbulence decays at different rates for each case until reaching the top of the boundary layer. The effect of the different surface temperature changes is also visible in the horizontally averaged temperature profiles. Both the 10 m/s and 15 m/s cases impose similar temperature changes (-1.4 K/hr and -1.5 K/hr, respectively) and similar temperatures at the ocean surface. However, the cooling effect in the very stable 10 m/s case is limited to z<350 m, similar to the veer and turbulence profiles.

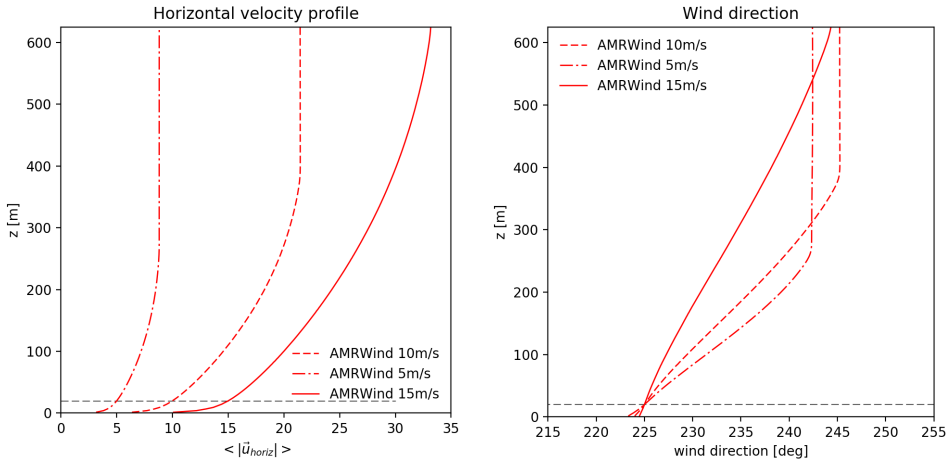

Fig. 8 Comparison of the horizontal wind speed and wind direction profile for the stable 5 m/s, 10 m/s, and 15 m/s boundary layers. The dashed horizontal line corresponds to the measurement height z=20 m.

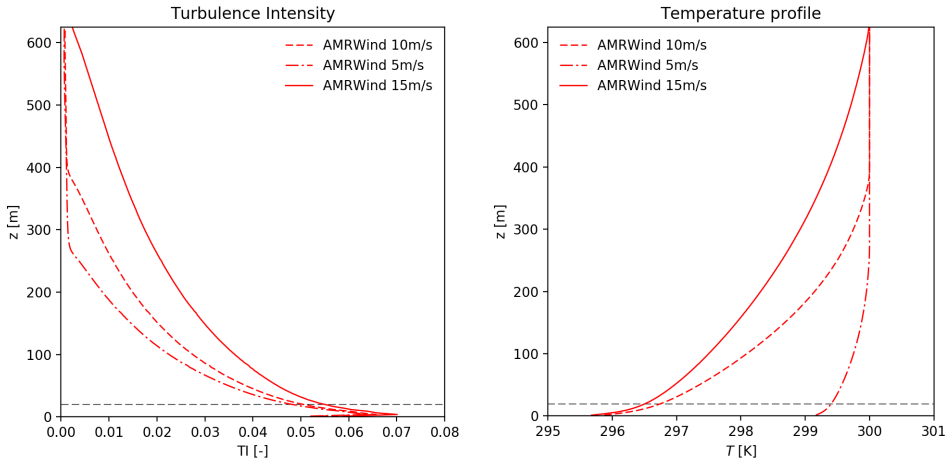

Fig. 9 Comparison of the turbulence intensity and temperature profile for the stable 5 m/s, 10 m/s, and 15 m/s boundary layers. The dashed horizontal line corresponds to the measurement height z=20 m.

3. Comparison with neutral and unstable conditions

Strong differences based on atmospheric stratification can also be seen when we compare the stable ABL cases with the neutral and unstable counterparts from [5]. In the previous study, both neutral and unstable offshore boundary layer cases were considered at the same 5 m/s, 10 m/s and 15 m/s wind speeds. Similar to the findings in IV.C.1, the 5 m/s and 10 m/s unstable cases were classified as "very unstable," while the 15 m/s was identified as "unstable" based on the Obukhov length scale.

The impact of the stability on the turbulent structures can be seen through the correlation statistics and calculated length scales in Figure 10 and 11. The large disparity between the size of the turbulent structures in the stable and neutral or unstable cases is immediately evident from the calculated $\langle R_{11}(\boldsymbol{\xi})\rangle$ coefficients. The longitudinal length scales for the unstable ABL cases can also be an order of magnitude larger than the stable ABL cases. The large lateral length scales for the very unstable ABL cases, compared to the smaller lateral length scales for the neutral and stable cases, is also worth noting. For the 5 m/s and 10 m/s very unstable ABL cases, the lateral dimensions of the turbulent structures are similar to the longitudinal length scale. This is consistent with the large convective structures which develop in those cases. For the unstable 15 m/s case, the lateral length scales were closer to neutral and stable cases.

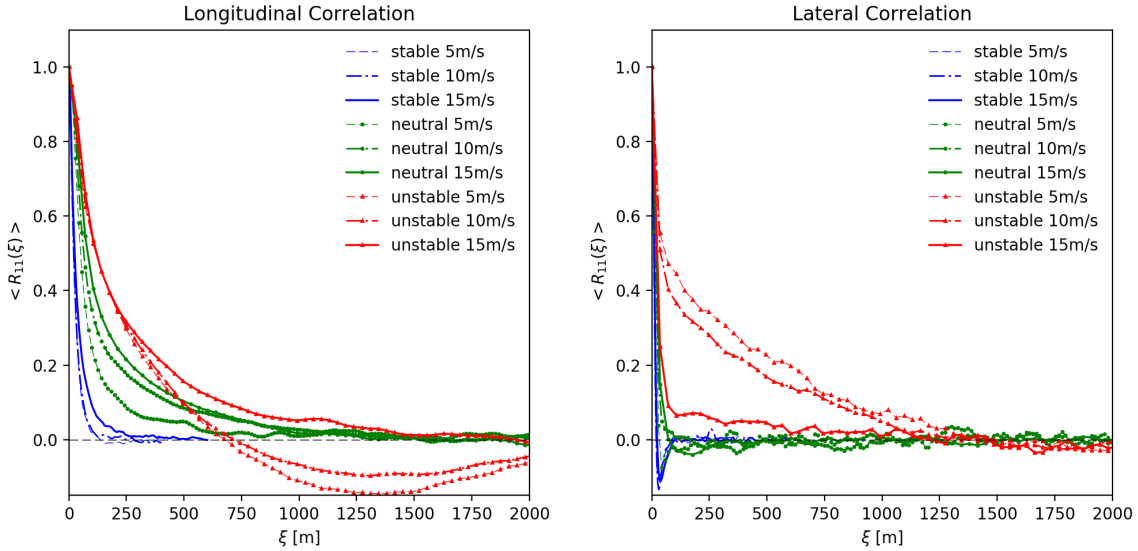

Fig. 10 Calculation of the averaged longitudinal and lateral $\langle R_{11}(\boldsymbol{\xi})\rangle$ coefficient at z=20 m for all ABL stability cases and windspeeds.

V. Conclusion

In this study, we have simulated the stable offshore boundary layer matching the characteristics of measurements from Nantucket Sound in the Northeastern United States. Three cases with wind speeds of 5 m/s, 10 m/s, and 15 m/s were selected, and simulations were performed using the ExaWind codes to match the TI and stability levels observed at the Cape Wind platform. When examining the effect of stratification using the Obukhov length, differences in the ABL behavior were seen between the very stable boundary layer cases (5 m/s and 10 m/s), and the stably stratified case (15 m/s). The very stable cases had shorter turbulent structures and less growth in the boundary layer compared to the 15 m/s case. The behavior of the three stable boundary layers was also compared to the neutral and unstable cases studied in [5]. As expected, the turbulent structures in all stable cases were noticeably smaller than in the neutral and unstable boundary layers.

In addition to these simulations, we also examined the domain and mesh requirements necessary to capture important physical features of the stable offshore boundary layers. Based on the calculated turbulent integral length scale, horizontal domain sizes of 750 m $\times$ 750 m were found to be necessary for these simulations. Various horizontal mesh resolutions were also considered for the stable runs, and it was determined that the finest resolution of Δ_x=2.5 m was able to resolve the longitudinal length scales and highest temporal frequencies, but inadequate for resolving the turbulence in the lateral

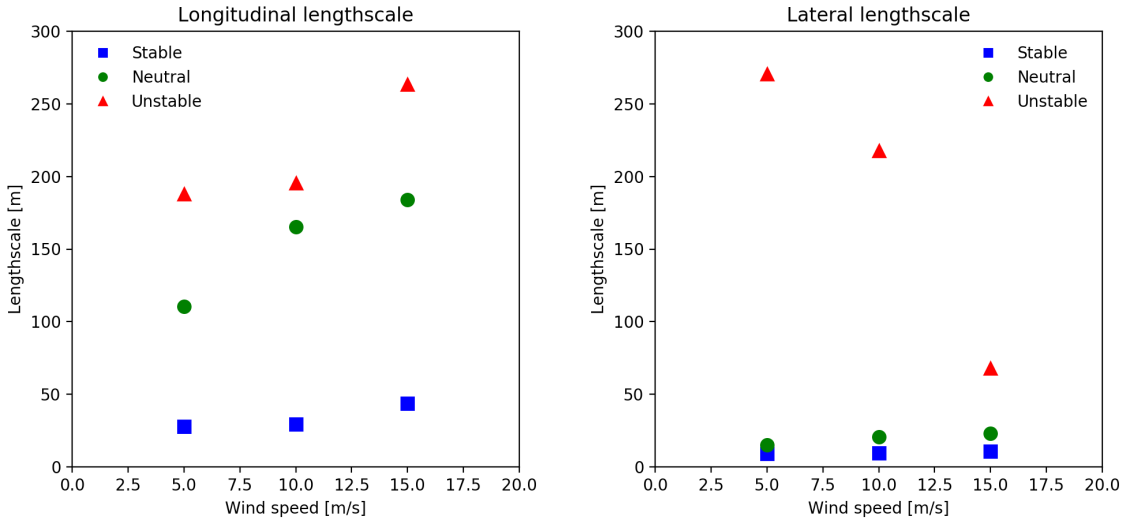

Fig. 11 Calculation of the averaged longitudinal and lateral length scale at z=20 m for all ABL stability cases.

direction. However, the possible effects of mesh anisotropy on the one equation turbulence model and the wall function treatment are not included in this work, and could be important for future simulations. We believe that further study is warranted to comprehensively determine the impact of stable stratification on the required mesh resolution.

Lastly, a comparison of the ExaWind solvers Nalu-Wind and AMR-Wind was conducted using the stable offshore boundary layer at 5 m/s. The mean statistics were found to agree well between the two LES codes. Small differences were found in wind profiles at higher elevations and for the peak S_u spectra, and excellent matches were observed for the averaged veer, temperature, and TI profiles. For the problem sizes considered here, it was also found that AMR-Wind was significantly more computationally efficient than Nalu-Wind when measured on a time per degree of freedom basis. However, the good agreement is a promising indication that the two codes can be used together effectively for future wind farm applications, where the highly efficient, structured nature of AMR-Wind handles the free stream boundary layer and is combined with the unstructured Nalu-Wind solver for complex turbine geometries.

Acknowledgments

The authors wish to acknowledge the contributions from M. Churchfield and S. Yellapantula for their development of the LES boundary conditions and for their efforts in validating the ExaWind codes.

This research was supported by the Wind Energy Technologies Office of the U.S. Department of Energy (DOE) Office of Energy Efficiency and Renewable Energy. Sandia National Laboratories is a multimission laboratory managed and operated by National Technology & Engineering Solutions of Sandia, LLC, a wholly owned subsidiary of Honeywell International Inc., for the U.S. Department of Energy's National Nuclear Security Administration under contract DE-NA0003525. The views expressed in the article do not necessarily represent the views of the U.S. Department of Energy or the United States Government.

This work was authored in part by the National Renewable Energy Laboratory, operated by Alliance for Sustainable Energy, LLC, for the U.S. Department of Energy (DOE) under Contract No. DE-AC36- 08GO28308. M. Brazell was funded by the Exascale Computing Project (17-SC-20-SC), a collaborative effort of two DOE organizations (Office of Science and the National Nuclear Security Administration).

A portion of the research was performed using computational resources sponsored by the DOE's Office of Energy Efficiency and Renewable Energy and located at the National Renewable Energy Laboratory.

References

[1] Nunalee, C. G., and Basu, S., "Mesoscale modeling of coastal low-level jets: implications for offshore wind resource estimation," *Wind Energy*, Vol. 17, No. 8, 2014, pp. 1199–1216. https://doi.org/https://doi.org/10.1002/we.1628.

[2] Pichugina, Y., Brewer, W., Banta, R., Choukulkar, A., Clack, C., Marquis, M., McCarty, B., Weickmann, A., Sandberg, S., Marchbanks, R., et al., "Properties of the offshore low level jet and rotor layer wind shear as measured by scanning Doppler Lidar," *Wind Energy*, Vol. 20, No. 6, 2017, pp. 987–1002. https://doi.org/https://doi.org/10.1002/we.2075.

[3] Archer, C. L., Colle, B. A., Veron, D. L., Veron, F., and Sienkiewicz, M. J., "On the predominance of unstable atmospheric conditions in the marine boundary layer offshore of the US northeastern coast," *Journal of Geophysical Research: Atmospheres*, Vol. 121, No. 15, 2016, pp. 8869–8885. https://doi.org/https://doi.org/10.1002/2016JD024896.

[4] Kaul, C. M., Ananthan, S., Churchfield, M., Mirocha, J. D., Berg, L. K., and Rai, R., "Large-eddy simulations of idealized atmospheric boundary layers using Nalu-Wind," *Journal of Physics: Conference Series*, Vol. 1452, IOP Publishing, 2020, p. 012078. https://doi.org/https://doi.org/10.1088/1742-6596/1452/1/012078.

[5] Cheung, L. C., Kaul, C. M., Hsieh, A. S., Blaylock, M. L., and Churchfield, M. J., "Large-eddy simulations of the Northeastern US coastal marine boundary layer," *Journal of Physics: Conference Series*, Vol. 1618, IOP Publishing, 2020, p. 062038. https://doi.org/https://doi.org/10.1088/1742-6596/1618/6/062038.

[6] Mason, P. J., and Derbyshire, S. H., "Large-Eddy Simulation of the Stably Stratified Atmospheric Boundary Layer," *Boundary-Layer Meteorology*, Vol. 53, 1990, p. 45.

[7] Brown, A., Derbyshire, S. H., and Mason, P. J., "Large-eddy simulation of stable atmospheric boundary layers with a revised stochastic subgrid model," *Q. J. R. Meteorol. Soc*, Vol. 120, 1994, p. 27.

[8] Andren, A., "The structure of stably stratified atmospheric boundary layers: a large-eddy simulation study," *Q. J. R. Meteorol. Soc*, Vol. 121, 1995, p. 24.

[9] Kemp, J. R., and Thompson, D. J., "Dispersion in stable boundary layers using large-eddy simulation," *Atmospheric Environment*, Vol. 30, No. 16, 1996, p. 12.

[10] Derbyshire, S. H., "Stable boundary-layer modelling: established approaches and beyond," *Boundary-Layer Meteorology*, Vol. 90, 1999, p. 23.

[11] Kosovic, B., and Curry, J. A., "A large eddy simulation study of a quasi-Steady, stably stratified atmospheric boundary layer," *Journal of Atmospheric Sciences*, Vol. 57, 2000, p. 16.

[12] Saiki, E. M., Moeng, C.-H., and Sullivan, P. P., "Large-eddy simulation of the stably stratified planetary boundary layer," *Boundary-Layer Meteorology*, Vol. 95, 2000, pp. 1–30.

[13] Beare, R. J., and Macvean, M. K., "Resolution sensitivity and scaling of large-eddy simulations of the stable boundary layer," *Boundary-Layer Meteorology*, Vol. 112, 2004, p. 24.

[14] Basu, S., Porté-agel, F., Foufoula-Georgiou, E., Vinuesa, J.-F., and Pahlow, M., "Revisiting the local scaling hypothesis in stably stratified atmospheric boundary-layer turbulence: an integration of field and laboratory measurements with large-eddy simulations," *Boundary-Layer Meteorology*, Vol. 119, No. 3, 2005, pp. 473–500. https://doi.org/10.1007/s10546-005-9036-2.

[15] Jimenez, M. A., and Cuxart, J., "Large-eddy simulations of the stable boundary layer using the standard Kolmogorov theory: range of applicability," *Boundary-Layer Meteorology*, Vol. 115, 2005, p. 20.

[16] Beare, R. J., Macvean, M. K., Holtslag, A. A. M., Cuxart, J., Esau, I., Golaz, J.-C., Jimenez, M. A., Khairoutdinov, M., Kosovic, B., Lewellen, D., Lund, T. S., Lundquist, J. K., McCabe, A., Moene, A. F., Noh, Y., Raasch, S., and Sullivan, P., "An Intercomparison of Large-Eddy Simulations of the Stable Boundary Layer," *Boundary-Layer Meteorology*, Vol. 118, No. 2, 2006, pp. 247–272. https://doi.org/10.1007/s10546-004-2820-6.

[17] Kumar, V., Kleissl, J., Meneveau, C., and Parlange, M. B., "Large-eddy simulation of a diurnal cycle of the atmospheric boundary layer: Atmospheric stability and scaling issues," *Water Resources Research*, Vol. 42, No. 6, 2006. https://doi.org/10.1029/2005wr004651.

[18] Lu, H., and Porté-Agel, F., "Large-eddy simulation of a very large wind farm in a stable atmospheric boundary layer," *Physics of Fluids*, Vol. 23, No. 6, 2011. https://doi.org/10.1063/1.3589857.

[19] Huang, J., and Bou-Zeid, E., "Turbulence and vertical fluxes in the stable atmospheric boundary layer. Part I: a large-eddy simulation study," *Journal of the Atmospheric Sciences*, Vol. 70, No. 6, 2013, pp. 1513–1527. https://doi.org/10.1175/jas-d-12-0167.1.

[20] Park, J., Basu, S., and Manuel, L., "Large-eddy simulation of stable boundary layer turbulence and estimation of associated wind turbine loads," *Wind Energy*, Vol. 17, No. 3, 2014, pp. 359–384. https://doi.org/10.1002/we.1580.

[21] Abkar, M., and Porté-Agel, F., "Influence of atmospheric stability on wind-turbine wakes: A large-eddy simulation study," *Physics of Fluids*, Vol. 27, No. 3, 2015. https://doi.org/10.1063/1.4913695.

[22] Stoll, R., and Porté-Agel, F., "Large-Eddy Simulation of the Stable Atmospheric Boundary Layer using Dynamic Models with Different Averaging Schemes," *Boundary-Layer Meteorology*, Vol. 126, No. 1, 2007, pp. 1–28. https://doi.org/10.1007/s10546-007-9207-4.

[23] van Dop, H., and Axelsen, S., "Large eddy simulation of the stable boundary-layer: a retrospect to Nieuwstadt's early work," *Flow, Turbulence and Combustion*, Vol. 79, No. 3, 2007, pp. 235–249. https://doi.org/10.1007/s10494-007-9093-3.

[24] Chow, F. K., and Zhou, B., "Large-eddy simulation of the stable boundary layer with explicit filtering and reconstruction turbulence modeling," *Journal of the Atmospheric Sciences*, Vol. 68, No. 9, 2011, pp. 2142–2155. https://doi.org/10.1175/2011jas3693.1.

[25] Matheou, G., "Numerical discretization and subgrid-scale model effects on large-eddy simulations of a stable boundary layer," *Quarterly Journal of the Royal Meteorological Society*, Vol. 142, No. 701, 2016, pp. 3050–3062. https://doi.org/10.1002/qj.2888.

[26] Sullivan, P. P., Weil, J. C., Patton, E. G., Jonker, H. J., and Mironov, D. V., "Turbulent winds and temperature fronts in large-eddy simulations of the stable atmospheric boundary layer," *Journal of the Atmospheric Sciences*, Vol. 73, No. 4, 2016, pp. 1815–1840.

[27] Aitken, M. L., Kosović, B., Mirocha, J. D., and Lundquist, J. K., "Large eddy simulation of wind turbine wake dynamics in the stable boundary layer using the Weather Research and Forecasting Model," *Journal of Renewable and Sustainable Energy*, Vol. 6, No. 3, 2014. https://doi.org/10.1063/1.4885111.

[28] Ghaisas, N. S., Archer, C. L., Xie, S., Wu, S., and Maguire, E., "Evaluation of layout and atmospheric stability effects in wind farms using large-eddy simulation," *Wind Energy*, Vol. 20, No. 7, 2017, pp. 1227–1240. https://doi.org/10.1002/we.2091.

[29] Wurps, H., Steinfeld, G., and Heinz, S., "Grid-resolution requirements for large-eddy simulations of the atmospheric boundary layer," *Boundary-Layer Meteorology*, Vol. 175, No. 2, 2020, pp. 179–201. https://doi.org/10.1007/s10546-020-00504-1.

[30] Moeng, C.-H., "A large-eddy-simulation model for the study of planetary boundary-layer turbulence," *Journal of the Atmospheric Sciences*, Vol. 41, No. 13, 1984, pp. 2052–2062.

[31] Etling, D., *Modelling the vertical ABL structure*, 1996, Chap. 2, pp. 45–86. https://doi.org/10.1142/9789814447164_0003, URL https://www.worldscientific.com/doi/abs/10.1142/9789814447164_0003.

[32] Sprague, M. A., Ananthan, S., Vijayakumar, G., and Robinson, M., "ExaWind: A multifidelity modeling and simulation environment for wind energy," *Journal of Physics: Conference Series*, Vol. 1452, No. 1, 2020. https://doi.org/10.1088/1742-6596/1452/1/012071.

[33] Domino, S. P., "Sierra Low {Mach} Module: Nalu Theory Manual 1.0," Tech. Rep. SAND2015-3107W, Sandia National Laboratories, 2015.

[34] Heroux, M., Bartlett, R., Howle, V., Hoekstra, R., Hu, J., Kolda, T., Lehoucq, R., Long, K., Pawlowski, R., Phipps, E., Salinger, A., Thornquist, J., Tuminaro, R., Willenbring, J., and Williams, A., "An overview of Trilinos," Tech. Rep. SAND-20032927, Sandia National Laboratories, Albuquerque, NM, 2003.

[35] Moen, C. D., and Domino, S. P., "A review of splitting errors for approximate projection methods," *16th AIAA Computational Fluid Dynamics Conference*, AIAA, Orlando, FL, 2003. https://doi.org/10.2514/6.2003-4236.

[36] Edwards, H., Williams, A., Sjaardema, G., Baur, D., and Cochran, W., "SIERRA Toolkit computational mesh computational model," Tech. Rep. SAND-20101192, Sandia National Laboratories, Albuquerque, NM, 2010.

[37] Zhang, W., Almgren, A., Beckner, V., Bell, J., Blaschke, J., Chan, C., Day, M., Friesen, B., Gott, K., Graves, D., Katz, M., Myers, A., Nguyen, T., Nonaka, A., Rosso, M., Williams, S., and Zingale, M., "AMReX: a framework for block-structured adaptive mesh refinement," *Journal of Open Source Software*, Vol. 4, No. 37, 2019, p. 1370. https://doi.org/10.21105/joss.01370, URL https://doi.org/10.21105/joss.01370.

[38] Almgren, A. S., Bell, J. B., Colella, P., Howell, L. H., and Welcome, M. L., "A conservative adaptive projection method for the variable density incompressible Navier–Stokes equations," *Journal of computational Physics*, Vol. 142, No. 1, 1998, pp. 1–46.

[39] Sverdrup, K., Nikiforakis, N., and Almgren, A., "Highly parallelisable simulations of time-dependent viscoplastic fluid flow with structured adaptive mesh refinement," *Physics of Fluids*, Vol. 30, No. 9, 2018, p. 093102. https://doi.org/https://doi.org/10.1063/1.5049202.

[40] Colella, P., and Woodward, P. R., "The Piecewise Parabolic Method (PPM) for gas-dynamical simulations," *Journal of Computational Physics*, Vol. 54, No. 1, 1984, pp. 174–201. https://doi.org/https://doi.org/10.1016/0021-9991(84)90143-8, URL http://www.sciencedirect.com/science/article/pii/0021999184901438.

[41] Taylor, P. K., and Yelland, M. J., "The dependence of sea surface roughness on the height and steepness of the waves," *Journal of physical oceanography*, Vol. 31, No. 2, 2001, pp. 572–590.